Continuous Recording of Resonator Characteristics Using Single-Sideband Modulation

Martin Lippmann *,†, Moritz Hitzemann †, Leonardo Hermeling, Kirsten J. Dehning, Jonas Winkelholz, Rene Wantosch and Stefan Zimmermann

Department of Sensors and Measurement Technology, Institute of Electrical Engineering and Measurement Technology, Leibniz Universität Hannover, Appelstr. 9A, 30167 Hannover, Germany; hitzemann@geml.uni-hannover.de (M.H.); hermeling@geml.uni-hannover.de (L.H.); dehning@geml.uni-hannover.de (K.J.D.); winkelholz@geml.uni-hannover.de (J.W.); rene.wantosch@stud.uni-hannover.de (R.W.); zimmermann@geml.uni-hannover.de (S.Z.)
* Correspondence: lippmann@geml.uni-hannover.de; Tel.: +49-511-762-14646
† These authors contributed equally to this work.

Abstract: Electrical resonators are usually characterized by their resonance frequency, attenuation and quality factor. External quantities can affect these parameters, resulting in a characteristic change in the resonator, which can be used as a sensor effect. This work presents a new concept and electronic device for the continuous recording of resonator characteristics using single-sideband modulation. A test signal consisting of a center frequency and two sidebands is generated and the center frequency is set close to the resonator's resonance frequency while the two sidebands are adjusted symmetrically around the center frequency. By exiting the resonator with the test signal and demodulating the resulting output into individual frequency components, a continuous measurement of the attenuation is possible. The center frequency is adjusted so that both sidebands have equal attenuation, resulting in a center frequency that corresponds to the resonance frequency of the resonator. If the resonator does not show a symmetrical frequency response, the sideband attenuation ratio can be adjusted accordingly. Continuous recording of the resonator characteristics at a sampling rate of 100 Sps was verified using a digitally tunable RLC series resonator with resonance frequencies between 250 MHz and 450 MHz, resulting in a maximum error below 1.5%.

Keywords: split-ring resonator; SRR; tracking electronics; readout electronics; demodulator; single sideband; SSB

1. Introduction

Resonators, such as split-ring resonators [1–12], are widely used in sensor applications to detect even the slightest changes in ambient conditions. The characteristic parameters of a resonator, namely its resonant frequency, the damping at resonance and its quality factor, can be measured using a vector network analyzer (VNA). The VNA records the frequency response by performing a defined frequency sweep and determining the scattering, from which the resonance frequency, quality factor and attenuation can be derived [1,13]. This results in a characteristic frequency response, from which the resonance frequency and attenuation can be derived. Depending on the VNA and measurement parameters, this method allows highly accurate determination of the resonator parameters, but it comes at the expense of measurement speed. However, this lack of measurement speed may not be suitable for applications requiring continuous monitoring, as the temporal resolution of the measurements achieved with a VNA is too low. To overcome this limitation, Hitzemann et al. [14] have developed simple electronics to continuously measure the attenuation of a resonator at a specific frequency. Any change in attenuation infers a shift in resonance frequency and/or attenuation and thus a variation in permittivity and/or conductivity of the split capacitor of a split-ring resonator (SRR). However, relying on a single frequency

limits the detectable frequency shift of the resonator and makes it difficult to attribute the measured attenuation to a change in resonance frequency or general attenuation.

Another approach to determining a resonator's characteristics involves measuring the exponential decay of a resonator excited to oscillation, which is often used for resonators such as quartz microbalances (QCMs) [15]. This method requires rapid and precise data acquisition operating at at least twice the resonator's resonance frequency to capture the exponential decay.

While various other techniques exist for low-frequency resonators like QCMs, as shown by Alassi et al. [16], limitations arise for higher-frequency resonators such as SRRs due to electronic component constraints.

Using SRRs as detectors in high-performance liquid chromatography (HPLC) and ion chromatography (IC) requires rapid sensor response and thus new concepts capable of fast, accurate and continuous tracking of the resonator's characteristics. In this case, a response time of 1 s or less is required to capture the narrow peaks eluting from the chromatographic column [8,9,17]. The same applies for various other applications, where SRRs are employed as sensing elements, e.g., fast analysis of liquids [2,4,7], the detection of biomarkers [5,6] and the identification of defects and cracks in metal objects [3]. This highlights the necessity for fast, accurate and continuous tracking of SRR characteristics.

A promising approach to determining the quality factor was outlined by Kuzikov et al. [18]. This approach determines the quality factor of a resonator from the signal of the reflection of two amplitude-modulated frequencies with equal amplitude.

Inspired by the Pound–Drever–Hall technique [19,20], which is based on measuring the phase change in the emitted light to a reference oscillator and subsequent control of the light source, a new concept using two simultaneously measured attenuations in the frequency response of the resonator has been proposed by Lippmann et al. [21]. A comparable methodology for tracking the resonance frequency has already been proposed in the field of atomic force microscopy [22–24] and is now to be transferred to the domain of electrical resonators, utilizing the concept presented in this work.

Concept of Continuous Recording of Resonance Frequency, Attenuation at Resonance and Quality Factor

The proposed concept for the continuous recording of the resonator characteristics relies on a transmission measurement with a periodic test signal $x_T(t) = x_T(t - nT)$, $n \in \mathbb{Z}$. The frequency spectrum $X_T(\mathrm{j}2\pi f)$ of this signal consists of a variable center frequency f_{CN} and two sidebands, symmetrically positioned around the center frequency with a frequency difference of f_{BW}. This results in the frequency of the lower sideband $f_{LSB} = f_{CN} - f_{BW}/2$ and the frequency of the upper sideband $f_{USB} = f_{CN} + f_{BW}/2$. Figure 1 shows the concept of the transmission measurement segmented into the signal generation, excitation of the SRR and analysis of the received signal. By separately analyzing the amplitude at these frequencies after transmission, the position of the test signal in the resonance curve can be derived.

In a first approximation, an SRR can be modeled by a damped RLC bandstop filter as shown in Figure 1b with the amplitude response $|G(\mathrm{j}2\pi f)|_{\mathrm{RLC}}$ according to Equation (1). A detailed derivation of this equation can be found in the Appendix A.

$$|G(\mathrm{j}2\pi f)|_{\mathrm{RLC}} = \frac{\sqrt{\left(f_0^2 - f^2\right)^2 + \left(f f_0 2D\right)^2}}{\sqrt{\left(f_0^2 - f^2\right)^2 + \left(\alpha f f_0 2D\right)^2}} \tag{1}$$

Here, f_0 represents the resonance frequency of the resonator and D the damping factor of the RLC series circuit, while α represents the relative attenuation of the resonator at resonance. The resonator would transmit the components of the test signal accordingly with $|G(\mathrm{j}2\pi f_{CN})|_{\mathrm{RLC}}$, $|G(\mathrm{j}2\pi f_{LSB})|_{\mathrm{RLC}}$ and $|G(\mathrm{j}2\pi f_{USB})|_{\mathrm{RLC}}$. For the calculation of the amplitude responses, a resonator based on the equivalent circuit diagram depicted in Figure 1b was used, assuming $f_0 = 500\,\mathrm{MHz}$, $D = 0.01$ and $\alpha = 2$. The two frequencies of the

sidebands were symmetrically centered around the center frequency f_{CN} with a constant bandwidth of $f_{BW} = 10$ MHz. Consequently, the frequencies of the two sidebands are directly dependent on the center frequency. Figure 2 illustrates the amplitude response for the lower sideband (LSB), the center frequency (CN) and the upper sideband (USB) relative to the center frequency.
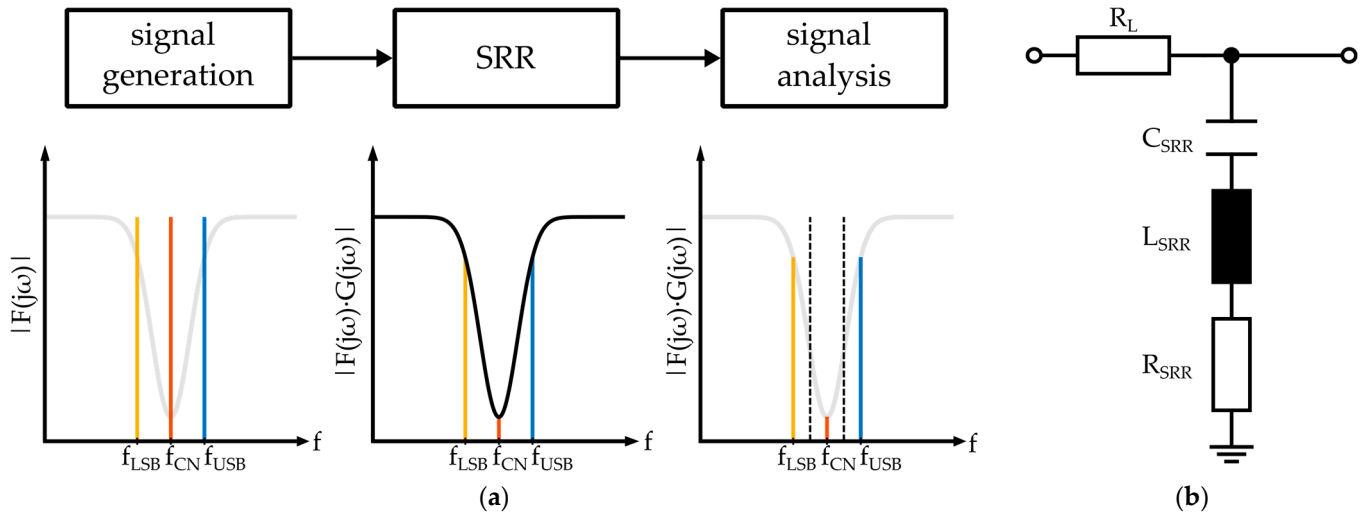
Figure 1. (**a**) Basic concept of the new tracking method based on a variable center frequency f_{CN} and the two sidebands f_{LSB} and f_{USB}. (**b**) Simplified equivalent circuit of a split-ring resonator (SRR).
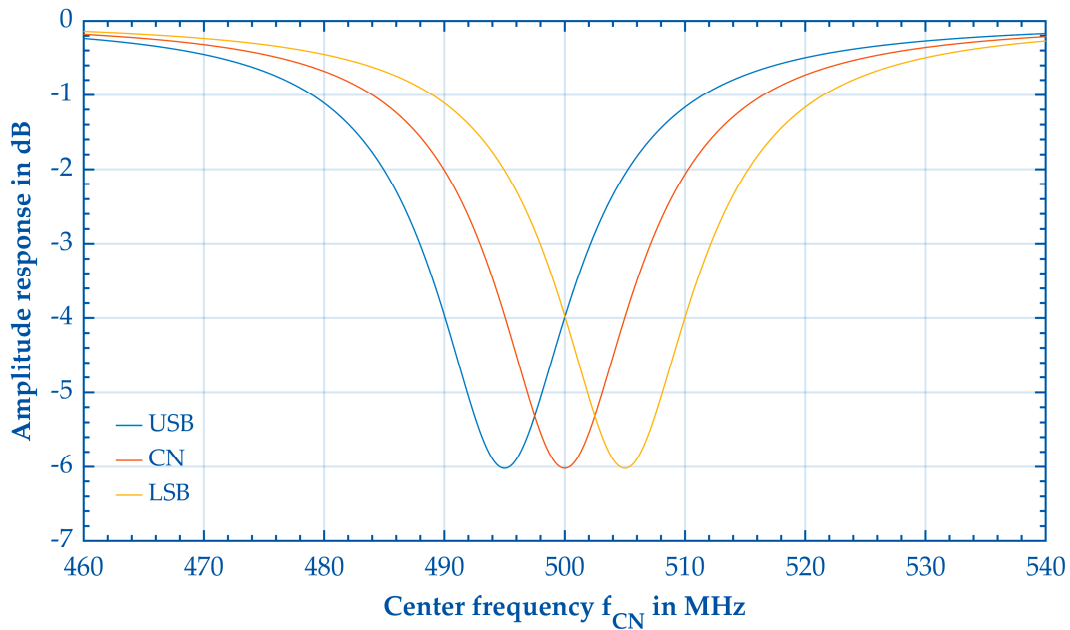
Figure 2. Attenuation at the center frequency f_{CN}, the lower sideband frequency f_{LSB} and the upper sideband frequency f_{USB} for a given center frequency f_{CN}.

At the intersection of the curves of the two sidebands, the attenuation of the sidebands is equal and $f_{CN} \approx f_0$. Under the condition that the sidebands are located left and right of the resonance frequency, a closer analysis of the transfer function $|G(j2\pi f)|_{RLC}$ shows that the value of this transfer function is always identical at the frequencies f_{LSB} and f_{USB} if

f_0 represents the geometric mean of these two frequencies. This relationship is defined by Equation (2).

$$0 < f_{\text{LSB}} < f_0 < f_{\text{USB}} \rightarrow \left(|G(\text{j}2\pi f_{\text{LSB}})|_{\text{RLC}} = |G(\text{j}2\pi f_{\text{USB}})|_{\text{RLC}} \leftrightarrow f_0 = \sqrt{f_{\text{LSB}} \cdot f_{\text{USB}}} \right) \quad (2)$$

If the ratio of the transfer function at f_{LSB} and f_{USB} is formed as shown in Equation (3), an error function $e(f_{\text{CN}})$ in decibels is obtained. This enables the adjustment of the test signal to the resonance frequency.

$$e(f_{\text{CN}}) = 20 \cdot \log\left(\frac{|G(\text{j}2\pi f_{\text{USB}})|_{\text{RLC}}}{|G(\text{j}2\pi f_{\text{LSB}})|_{\text{RLC}}} \right) \quad (3)$$

Figure 3 shows the influence of the parameters f_{BW}, f_0, D and α on this error function.
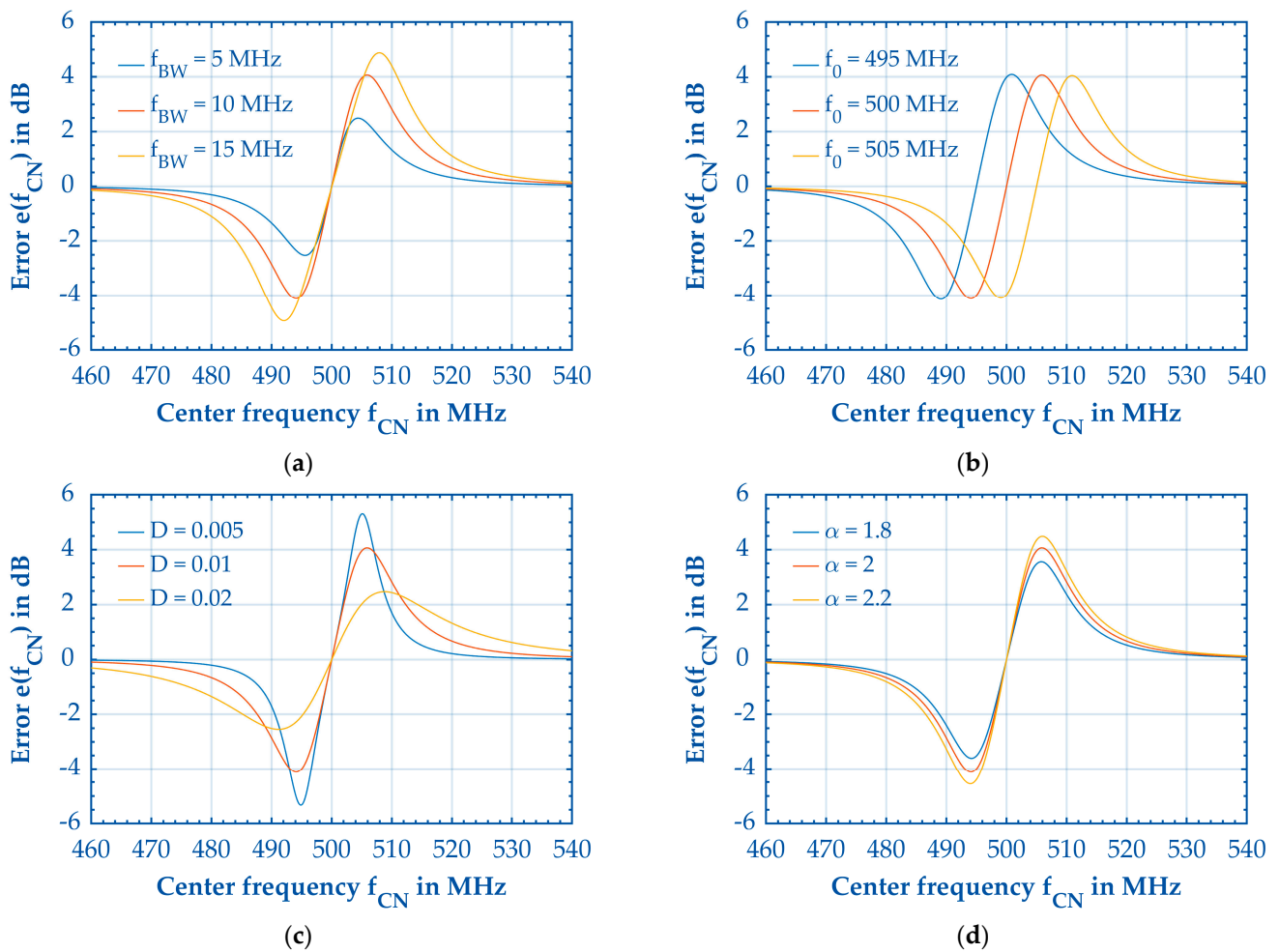
Figure 3. Influence of f_{BW} (**a**), f_0 (**b**), D (**c**) and α (**d**) on the error function.

Unlike α and D, only f_0 and f_{BW} affect the zero crossing of the curve. However, the effect of f_{BW} is very small and thus not visible in the figure. The frequency $f_{\text{CN},0}$ at which the error curve intersects the abscissa can be derived from Equation (4).

$$f_{\text{CN},0} = \sqrt{f_0^2 + f_{\text{BW}}^2/4} \quad (4)$$

Equation (4) shows that $f_{\text{CN},0}$ depends solely on the resonance frequency f_0 and the configured bandwidth f_{BW} of the test signal. Consequently, changes in the damping D and the damping coefficient α do not affect the position of $f_{\text{CN},0}$. This makes the presented

method suitable for damping-independent tracking of the resonance frequency. In other words, resonance frequency and damping can be derived independently, which is the major benefit compared to Hitzemann et al. [14]. In addition, it is notable that the error curve exhibits an approximately linear trajectory around the intersection point on the abscissa. Thus, within this frequency range, the linear system behavior of the system can be inferred. Assuming negligible distortions of the test signal resulting from changes in the SRR transmission behavior, this linear behavior facilitates using a linear controller for tracking this point. The operating range of the controller is thereby limited by the two extreme points around the abscissa interception point. This also defines the maximum detectable change $\Delta f_{0,\max}$ of the resonance frequency within a sampling interval ΔT_s. The concept presented can also be applied to resonators with a non-symmetrical amplitude response, as the discrepancy between f_{CN} and f_0 can be rectified by first measuring the non-symmetrical frequency response of the resonator and then using individual frequencies for the lower and upper sidebands or keeping symmetrical sidebands and adjusting the targeted amplitude ratio of the sidebands for $f_{CN} = f_0$. Assuming that the non-symmetrical frequency response remains constant over a certain frequency range, the accuracy of the measurement method is comparable to the results obtained with symmetrical resonators. As the primary focus of this work is on the basic concept, this is not discussed in detail here.

2. Materials and Methods

To implement the concept described above, custom-designed electronics have been developed to generate and split the high-frequency test signal into its frequency components. Illustrated in Figure 4a, the concept operates by first generating an intermediate-frequency (IF) test signal, which is then upconverted to the resonance frequency range of the resonator through single-sideband (SSB) modulation. Following transmission, the test signal is downconverted to a consistent IF range, aligning with the superheterodyne principle. Notably, this frequency range is identical to the frequency range from which the test signal was initially upconverted. Each stage of the modulation process is shown in Figure 4b.

The superheterodyne principle, with its constant IF range, has the advantage of avoiding variable filters for separating the frequency components when the test signal is shifted in the frequency range. Additionally, this method facilitates the use of a consistent high-frequency carrier signal for both upconversion and downconversion processes, ensuring coherence in signal processing. This means that for tracking the resonance frequency, only the frequency of the carrier signal S_{LO} needs to be adjusted according to $e(f_{CN})$ whenever the attenuations of the sidebands deviate from each other, simplifying the control process considerably.

Using single-sideband (SSB) modulation [22] eliminates the need for a filter before the downconversion mixer, which would be essential in scenarios involving amplitude modulation (AM) or double-sideband-suppressed carrier (DSSC) modulation for upconversion. By avoiding this filter, the test signal can be shifted over a wide frequency range, making it possible to track the frequency over a wide frequency range.

The final analysis of the separated signal components and the subsequent adjustment of the high-frequency carrier signal were carried out digitally on a measuring computer.

The IF test-signal generation and conversion into the high-frequency range mainly relied on the Weaver method [25] with minor modifications. As shown in the upper signal path in Figure 5, the first step is the amplitude modulation of a baseband signal s_{BB} with an IF frequency carrier signal $s_{IF,I}$ using the MC1496 mixer (On Semiconductor, Phoenix, AZ, USA). s_{BB} represents a simple cosine signal that is generated by an DDS AD9914 (Analog Devices, Wilmington, NC, USA). The frequency f_{BB} can be varied in a range from 0 MHz to 10.7 MHz.
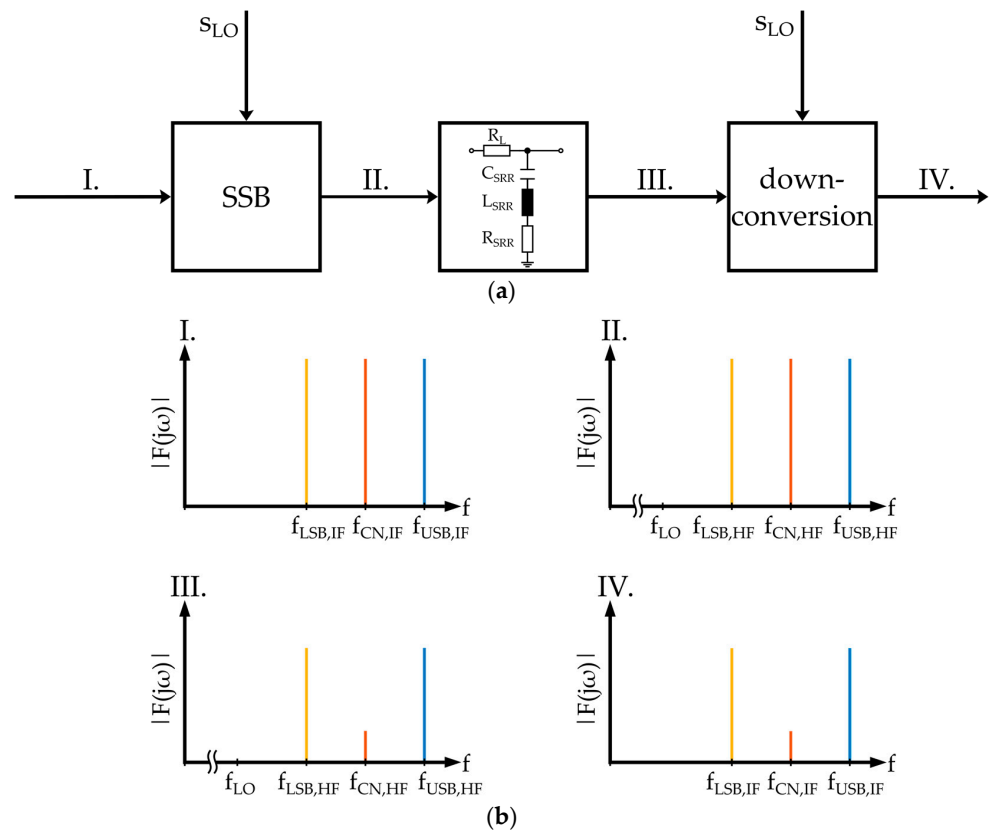
Figure 4. The figure illustrates the generation of the test signal, its transmission through the SRR and the downstream downconversion. Figure (**a**) depicts the individual frequency spectrum in each phase of the concept, commencing with the test signal before upconversion, the test signal frequency spectrum, the frequency spectrum after the SRR and finally, the downconversion. Figure (**b**) shows the frequency spectrum prior to the SSB modulation (I), after the SSB modulation (II), following the damping of the SRR (III), and after the downconversion (IV).
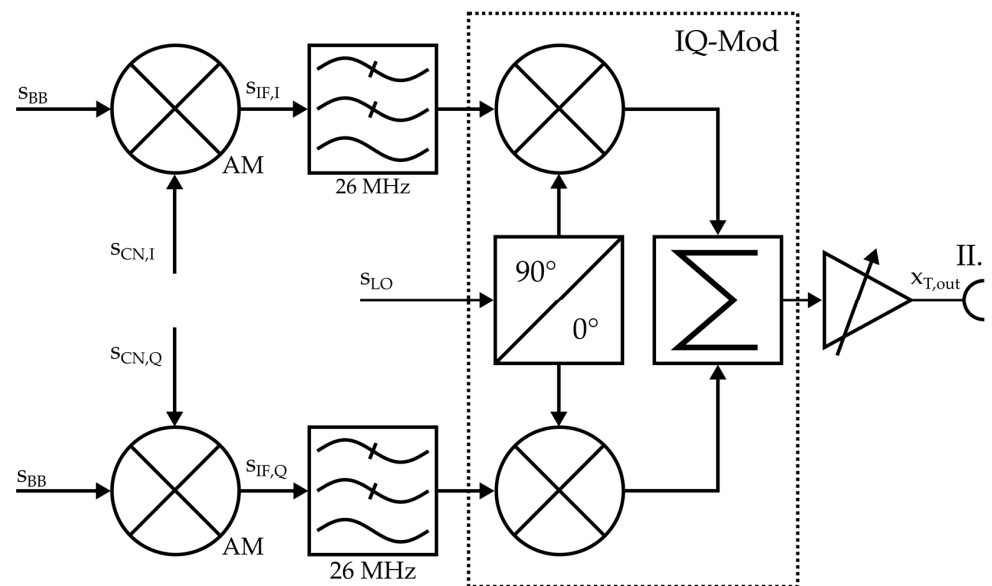
Figure 5. Schematic representation of the generation of the test signal $x_{T,out}$ by an IQ modulation of the IF signals $s_{IF,I}$ and $s_{IF,Q}$ generated by using a modified Weaver method from the signals s_{BB}, $s_{CN,I}$ and $s_{CN,Q}$.

$s_{\mathrm{CN,I}}$ is also a simple cosine signal, with a fixed frequency at $f_{\mathrm{CN}} = 10.7$ MHz derived via a divide-by-four, 50% duty cycle Johnson counter [26,27], which also generates the quadrature signal $s_{\mathrm{CN,Q}}$ corresponding to $s_{\mathrm{CN,I}}$. For this purpose, a flip-flop SN74HCS74DR (Texas Instruments, Dallas, TX, USA) was used. The rectangular output signals of the flip-flop were converted into cosine signals with the ECS-10.7-30A (ECS Inc., Lenexa, AR, USA) crystal filter, and afterwards amplified and filtered by an active all-pass filter for fine-tuning of the phase shift.

The product of the amplitude modulation is thereby the IF test signal $s_{\mathrm{IF,I}}$, whose spectrum corresponds qualitatively to that in Figure 4b and consists of the following signal components:

$$s_{\mathrm{IF,I}}(t) = \underbrace{A \cdot \cos(2\pi(f_{\mathrm{CN}} - f_{\mathrm{BB}})t + \varphi_{\mathrm{a}})}_{lower\ IF-sideband} + \underbrace{B \cdot \cos(2\pi f_{\mathrm{CN}}t + \varphi_{\mathrm{b}})}_{IF-center} + \underbrace{C \cdot \cos(2\pi(f_{\mathrm{CN}} + f_{\mathrm{BB}})t + \varphi_{\mathrm{c}})}_{upper\ IF-sideband} \tag{5}$$

While the IF carrier signal $s_{\mathrm{IF,I}}$ and the upper IF sideband are typically undesired in the conventional Weaver method and therefore suppressed, here, they serve as essential components of the final test signal. The low-pass filter shown in Figure 5 is only required to suppress the unwanted IF frequency carrier signal harmonics at the output of the mixer.

In the lower signal path of Figure 5, s_{BB} is mixed with the quadrature signal $s_{\mathrm{CN,Q}}$ of the IF carrier signal, resulting in the signal $s_{\mathrm{IF,Q}}$ with signal components showing a phase shift of 90° with respect to the signal components of $s_{\mathrm{IF,I}}$. Both the $s_{\mathrm{IF,I}}$ and the $s_{\mathrm{IF,Q}}$ are then upconverted to the frequency range of the resonator's resonance frequency by mixing the $s_{\mathrm{IF,I}}$ and the $s_{\mathrm{IF,Q}}$ with the high-frequency carrier signal s_{LO} in the IQ modulator ADL5385 (Analog Devices, Wilmington, NC, USA). s_{LO} is generated using a setup proposed by Hitzemann et al. [14] with a phase-locked loop (PLL) MAX2871 (Analog Devices, Wilmington, NC, USA). Due to the phase relationship between $s_{\mathrm{IF,I}}$ and $s_{\mathrm{IF,Q}}$, the lower sideband of the mixing products is suppressed when the upconverted signals are superimposed at the end of the IQ modulator. Thus, the upconversion with the IQ modulator effectively increases the frequency of all signal components of $s_{\mathrm{IF,I}}$ by the frequency f_{LO} of the carrier signal s_{LO}. After SSB modulation, the test signal $x_{\mathrm{T,out}}$ is post-amplified and provided to an SMA socket for the transmission measurement.

Following the transmission through the resonator, the transmitted signal $x_{\mathrm{T,in}}$ is first amplified by the amplifier ADL5330 (Analog Devices, Wilmington, NC, USA) and then downconverted into the IF range through mixing with s_{LO} using the mixer AD8342 (Analog Devices, Wilmington, NC, USA), as shown in Figure 6. Subsequently, the signal components are separated from each other to determine their amplitudes.

Separation of the IF center s_{CN} is straightforward; given its fixed frequency at 10.7 MHz, a narrow-band crystal filter can be used that is identical to the one employed after the Johnson counter, generating $s_{\mathrm{CN,Q}}$ and $s_{\mathrm{CN,I}}$. To isolate the two sidebands, suppression of the IF center is necessary using a bandstop filter. Subsequently, the lower sideband s_{LSB} is separated from the other signal components using an active low-pass filter. However, the separation of the upper sideband s_{USB} poses a different challenge. While theoretically possible with a suitable bandpass filter, an alternative approach was adopted here to enable the phase comparison of the sidebands, reserved for future exploration.

In our setup, the signal with a suppressed IF center underwent mixing with a cosine signal with twice the frequency of the IF center. This cosine signal, generated by a phase-locked loop (PLL) utilizing the isolated IF center signal as a reference, output a signal with doubled frequency. The subsequent crystal filter transformed the square wave signal from the PLL into a sine wave signal for the mixer. Consequently, the mixing process caused a spectrum inversion of the input signal so that the amplitude information of the upper sideband was then present in the output signal at the frequency of the original lower sideband. This allowed the same low-pass filter as that used for separating the lower sideband to be used. Finally, the amplitudes of the separated signal components were analyzed by converting all signals into equivalent DC voltages using the logarithmic amplifier AD8310

(Analog Devices, Wilmington, NC, USA), which were then finally digitized by the ADC AD7175 (Analog Devices, Wilmington, NC, USA). A photo of the tracking electronics is shown in Figure A1.
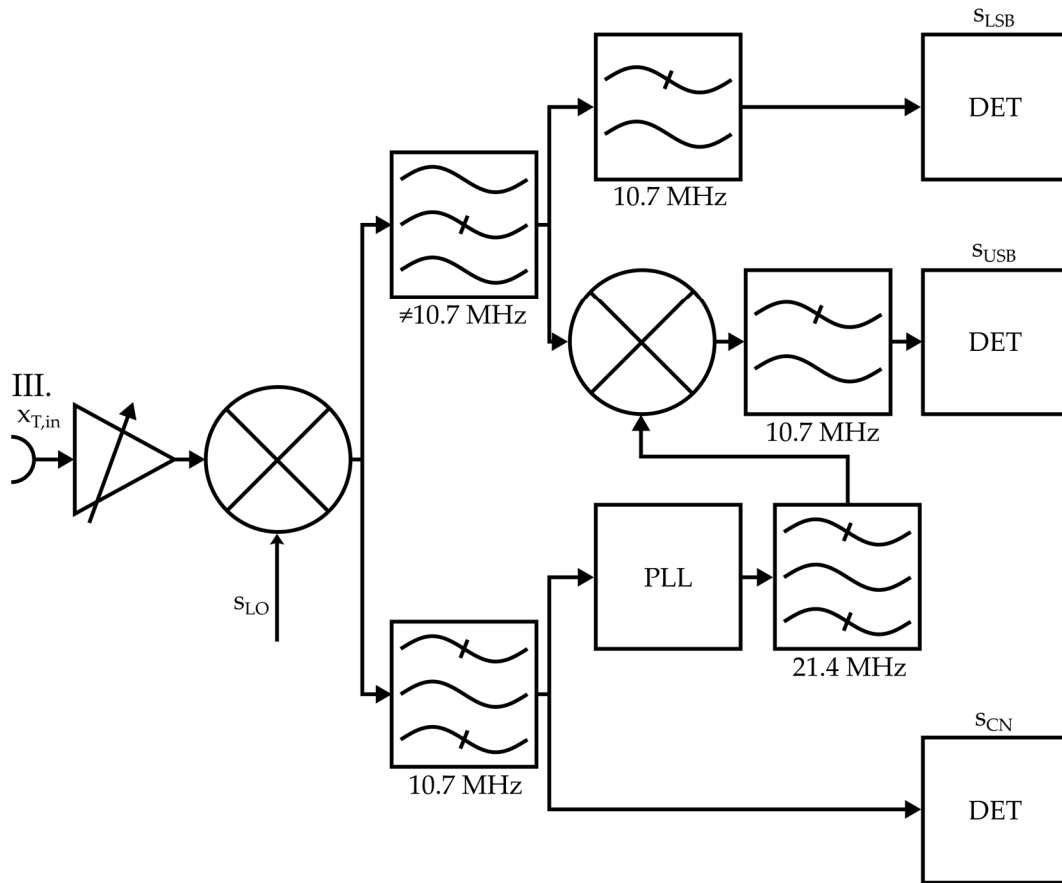
Figure 6. Block diagram of the downconversion electronics, including filtering and detection of each individual frequency component s_{LSB}, s_{USB} and s_{CN}.

A bandstop filter based on the circuit depicted in Figure 7a was developed as a resonator dummy for testing the tracking electronics. While the inductance L was set at a fixed value of 68 nH, the series-connected capacitance C_{SRR} was provided by the digitally tunable capacitor (DTC) PE64904 (pSemi, San Diego, CA, USA). In this configuration, R_1 and R_2 were not assigned a fixed value and were only present in the form of parasitic resistors. This resonator dummy allowed for 32 different amplitude responses, spanning a resonance frequency ranging from 252 MHz to 459 MHz for the bandstop filter. Figure 7b shows a photo of the resonator dummy.

Before using the developed resonator dummy, it was tested using a Through–Open–Short–Match (TOSM)-calibrated VNA ZNL6 (Rohde & Schwarz, Munich, Germany) with matching cables ZV-Z192 (Rohde & Schwarz, Munich, Germany). For the calibration of the VNA, a matching calibration kit ZN-Z23 (Rohde & Schwarz, Munich, Germany) was used. Therefore, each of the 32 different amplitude responses of the resonator dummy were recorded. Afterwards, the tracking electronics were tested in conjunction with the resonator dummy to evaluate the new concept of continuously recording the resonator's characteristics. For this purpose, the resonator dummy was connected to the tracking electronics with 25 cm long SMA cables 135101-01-M0.25 (Amphenol RF, Houten, The Netherlands). Some of the measurements were repeated with 50 cm long SMA cables 135101-01-M0.50 (Amphenol RF, Houten, The Netherlands). The complete measurement

setup containing the tracking electronics, the microcontroller board and the resonator dummy is shown in Figure A2.

(**a**)   (**b**)
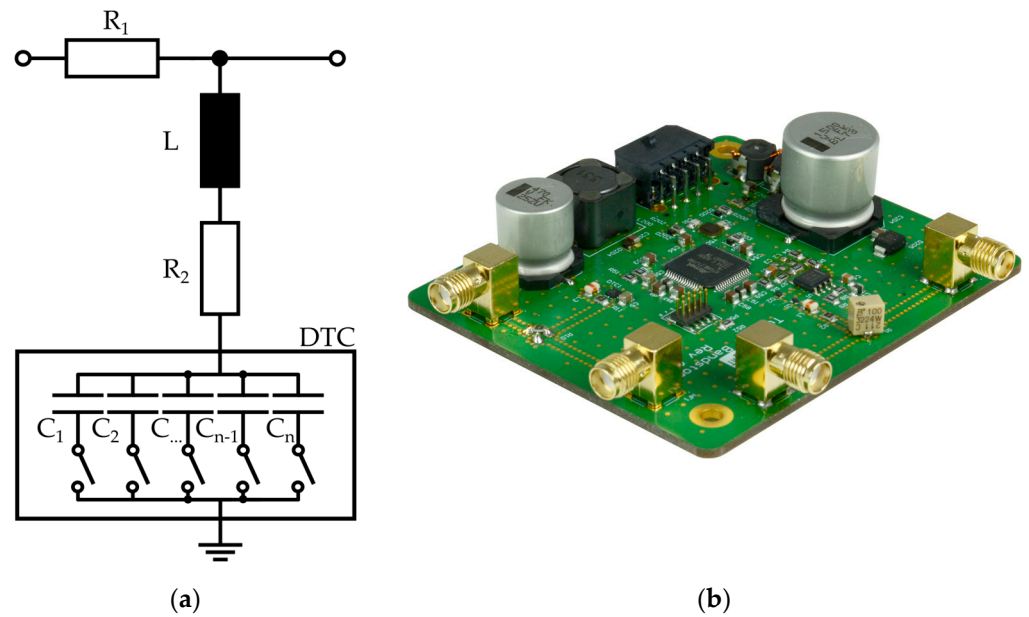
Figure 7. (**a**) Schematic of the RLC test resonator using a digitally tunable capacitor (DTC) for setting defined resonance frequencies, (**b**) photo of the assembled resonator with 32 adjustable resonance frequencies.

3. Results and Discussion

For clarity, Figure 8 shows the amplitude response of just every other DTC setting. The resonance frequency of the adjustable resonator dummy varies between 250 MHz and 460 MHz, depending on the DTC settings. The maximum attenuation is observed at the highest capacitance, with an attenuation of approximately −18 dB at resonance and a quality factor of 27.7. As the capacitance decreases, the attenuation at resonance drops to around −13 dB.
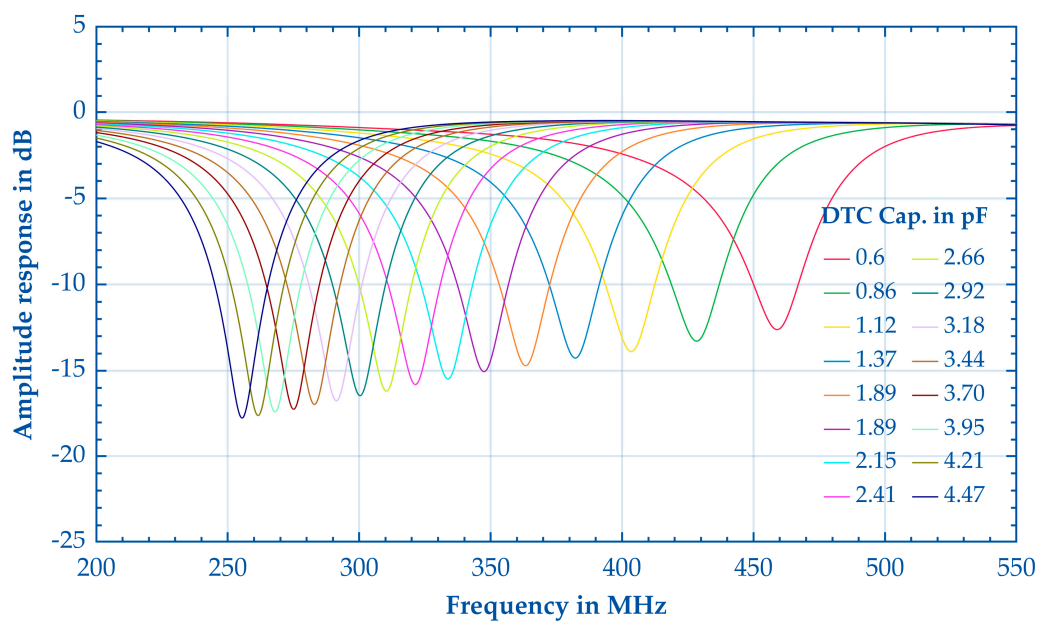
Figure 8. The amplitude responses of the adjustable resonator dummy at different DTC settings were measured with a TOSM-calibrated VNA ZNL6 (Rohde & Schwarz).

In order to test the tracking electronics, the amplitude responses of the adjustable resonator dummy were also recorded with the tracking electronics (in the same way as with the VNA). For this purpose, the center frequency of the test signal was swept over the frequency range shown, and the attenuation of the center frequency was recorded. The amplitude responses were recorded for all 32 settings of the resonator dummy. Figure 9 shows the amplitude response of just every other DTC setting as in Figure 8.
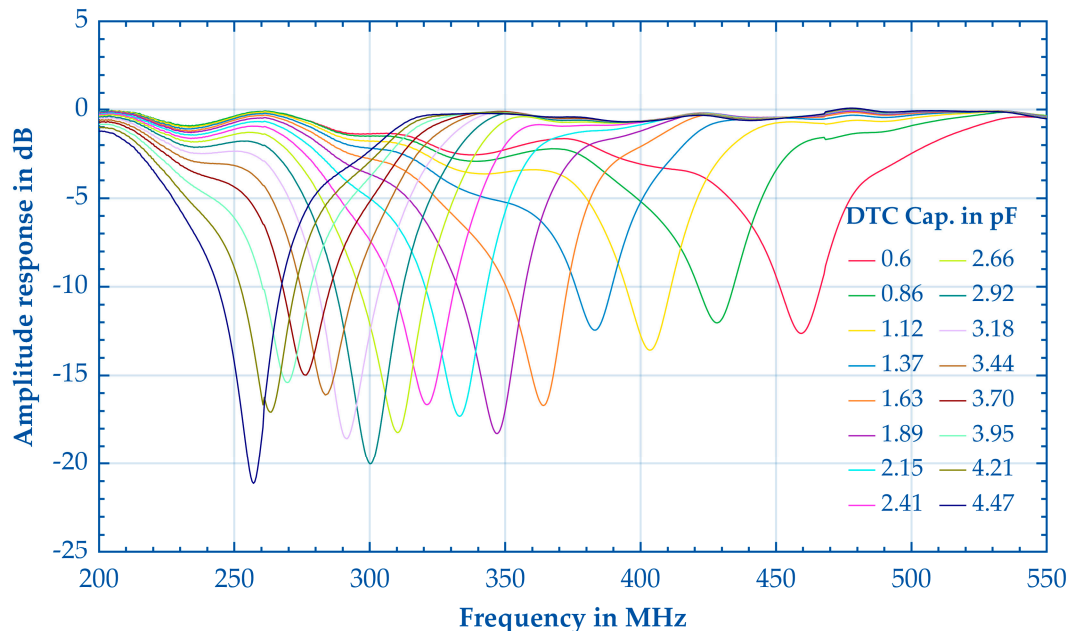
Figure 9. Amplitude responses of the adjustable resonator dummy at different DTC settings were measured with the tracking electronics connected with two 25 cm SMA cables.

Despite notable deviations in the attenuation curves compared to the VNA measurements in Figure 8, the qualitative shift in resonance frequency remains similar. The measurements reveal a maximal error of 1.5 MHz, corresponding to a relative error of less than 0.6% within the lower frequency range. With increasing frequencies, there is a reduction in both absolute and relative errors. Specifically, for the DTC capacitance of 0.6 pF, the error is only 59 kHz, leading to a relative error of only 13 ppm.

In order to investigate the deviations from the measurements with the VNA, the output power of the tracking electronics was measured. As depicted in Figure A3, the output power remains constant at approximately −15 dBm across the entire frequency range, with a slight decrease towards higher frequencies of about 0.5 dBm. The influence of this slight decrease on the observed deviation can be considered negligible. Likewise, the amplitude response measured on an attenuation element with a constant damping factor of −15 dB, as shown in Figure A4, exhibits no significant deviation from the expected −15 dB across the entire frequency range. In contrast, using longer cables (50 cm) connecting the resonator dummy to the tracking electronics yielded differing attenuation results, as depicted in Figure A5. Furthermore, a comparison of the impedance measurements of the Z_{11} parameter between the resonator dummy terminated with 50 ohms, from the calibration kit, as shown in Figure A6, and, alternatively, coupled with the demodulation stage of the tracking electronics, as shown in Figure A7, reveals that the demodulation stage induces additional deviation in the impedance curve, resulting from additional reflections of the test signal. As depicted in Figure A8, the input impedance of the demodulation stage of the tracking electronics is approximately 56 ohms at 200 MHz and drops to approximately 38 ohms over the frequency range up to 550 MHz. Therefore, it can be assumed that reflection-induced errors lead to the observed deviation in attenuation compared to the VNA.

Next, the amplitude response of the resonator dummy using a capacitance value of the DTC of 0.6 pF was recorded for the lower and upper sidebands generated with the tracking electronics. Figure 10a illustrates the amplitude response for the lower sideband (yellow), the center frequency (orange) and the upper sideband (blue) plotted against the set center frequency, as in Figure 2. The resonance frequency of the dummy resonator in this measurement was 459.259 MHz.
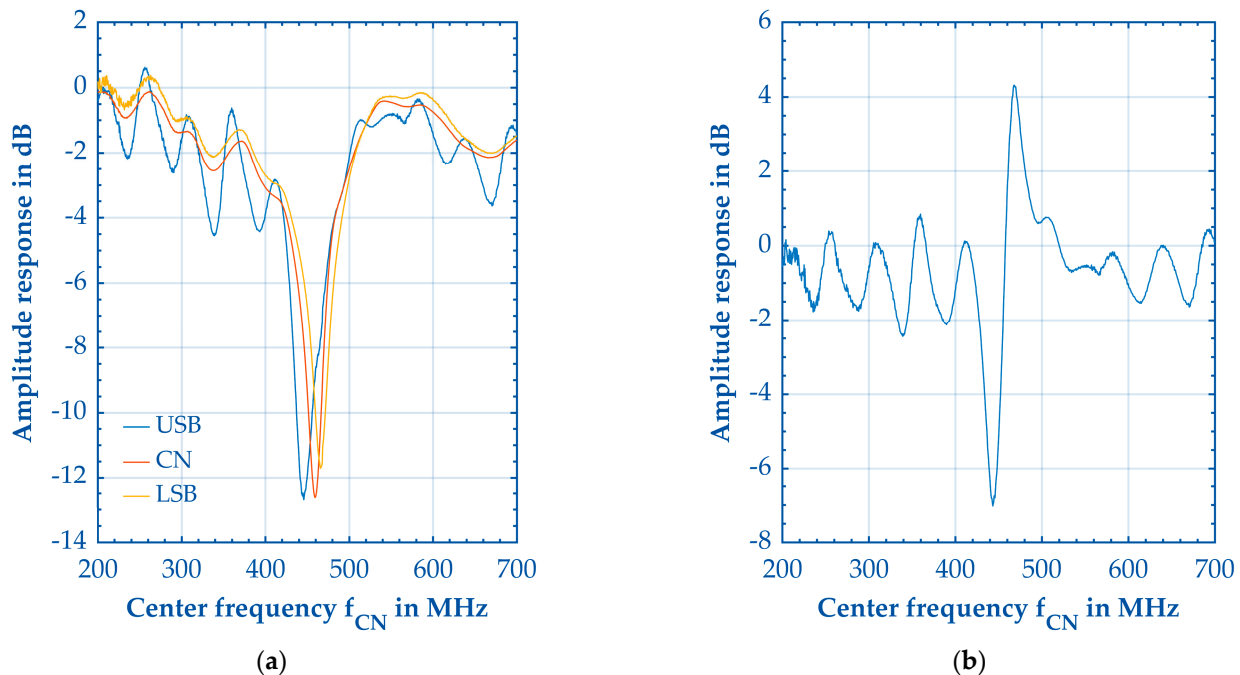
Figure 10. (**a**) Amplitude responses of the adjustable resonator dummy for the lower sideband (LSB), the center frequency (CN) and the upper sideband (USB) measured at 0.6 pF capacitance of the DTC settings; (**b**) the error signal derived from the lower and the upper sideband.

In this case, the minimum of the upper sideband is observed at a center frequency of 445.746 MHz, while the minimum for the lower sideband is reached at a center frequency of 465.766 MHz with a set frequency difference of 12.84 MHz between the sidebands generated by the tracking electronics. Consequently, a discrepancy of 0.507 MHz between the minimum of the lower sideband and the theoretically expected value results and a discrepancy of 7.513 MHz between the upper sideband and the theoretically expected value were found. Across the investigated frequency range, the mean deviation of the upper sideband from the theoretically expected value is 1.277 MHz; for the lower sideband, it is 0.334 MHz.

Furthermore, it is also evident that the maximum attenuation of the lower sideband is less than that of the upper sideband and the center frequency, while the upper sideband exhibits clear oscillations outside the resonance frequency of the resonator dummy.

Figure 10b plots the error signal derived from both the upper and lower sidebands against the center frequency. The curve shows the linear range of the error signal between the minimum at 443.243 MHz and the maximum at 468.268 MHz. The observed waves outside the linear range are artifacts resulting from the non-optimal measurement of the upper sideband. However, this does not impede the feasibility of resonance frequency tracking, as the resonance frequency is constrained within the linear range during tracking mode and thus prevented from shifting outside the linear range.

Due to the capability of measuring a shift in the resonance frequency despite the deviations observed in the amplitude responses, the setup remains suitable for validating the concept of resonance frequency tracking. To demonstrate the feasibility of resonance frequency tracking, the resonator dummy was first set to the setting with the lowest

resonance frequency and the test signal of the tracking electronics was adjusted accordingly. Subsequently, the 32 settings of the DTC were systematically cycled through, first in ascending and then in descending order, with each step lasting for 4 s.

Figure 11 compares the value of the set resonance frequencies (orange), which were previously determined with the tracking electronics (Figure 9), and the resonance frequency determined by the tracking electronics in resonance frequency tracking mode (blue). As expected, the tracking electronics readjusted the center of the test signal to match the new resonance frequency of the adjustable resonator dummy when the DTC setting was altered and only minor deviations from the designated resonance frequency were observed. The observed discrepancies are likely attributable to the differing attenuation of the upper and lower sidebands, as shown in Figure 10. Consequently, the error curve, with its 0 dB value, does not correspond precisely to the theoretically expected frequency $f_{CN,0}$, resulting in slight discrepancies when leveling.
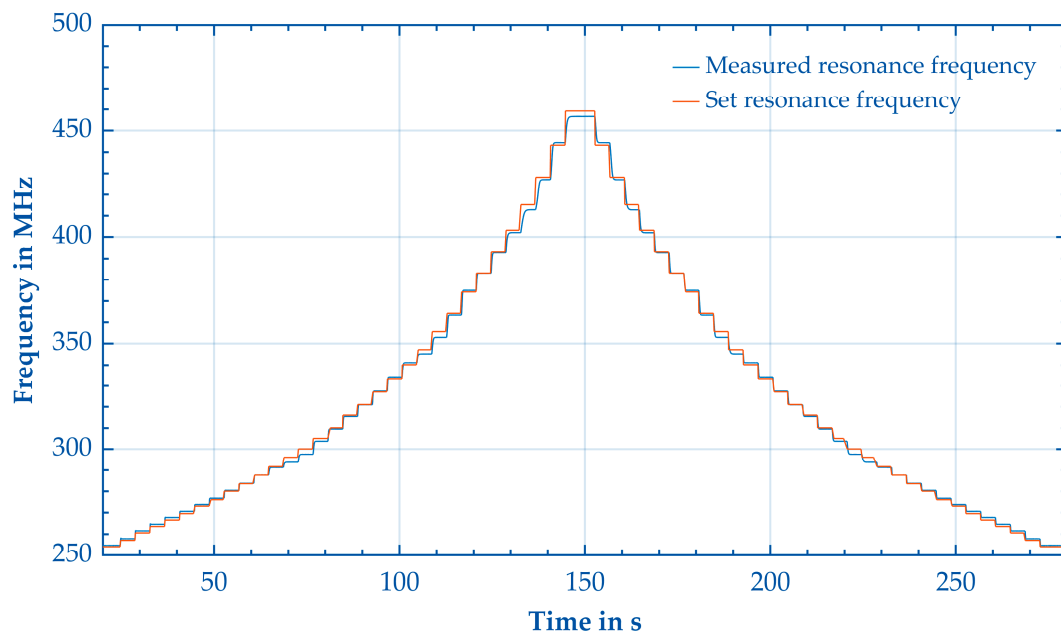
Figure 11. Tracking of resonance frequency over time using all 32 settings of the adjustable resonator dummy's DTC for 4 s each.

The discrepancies between the expected resonance frequency and the resonance frequency determined by the tracking electronics in resonance frequency tracking mode are illustrated in Figure A8. The observed discrepancies range from -3.7 MHz to $+1.2$ MHz, with even the greatest discrepancy corresponding to a relative error of less than 1.5%.

Finally, the same measurement was used to check whether the change in the damping parameters D and α could also be detected with the tracking electronics. Alongside monitoring the attenuation of the sidebands, the attenuation of the center frequency was also measured during resonance frequency tracking. This allowed three data points for a non-linear fit of Equation (1) to be acquired, enabling the calculation of an approximation of the parameters D and α. The current center frequency is taken as the resonance frequency, which corresponds to Equation (4) under the condition of $f_0^2 \gg f_{BW}$.

As a reference, the two parameters were determined using the fits of the amplitude responses from the measurements shown in Figure 9. While Figure 12a shows the approximated damping coefficient D (blue) compared to the true damping coefficient D (orange), Figure 12b shows the approximated damping coefficient α compared to the true damping coefficient α (orange).
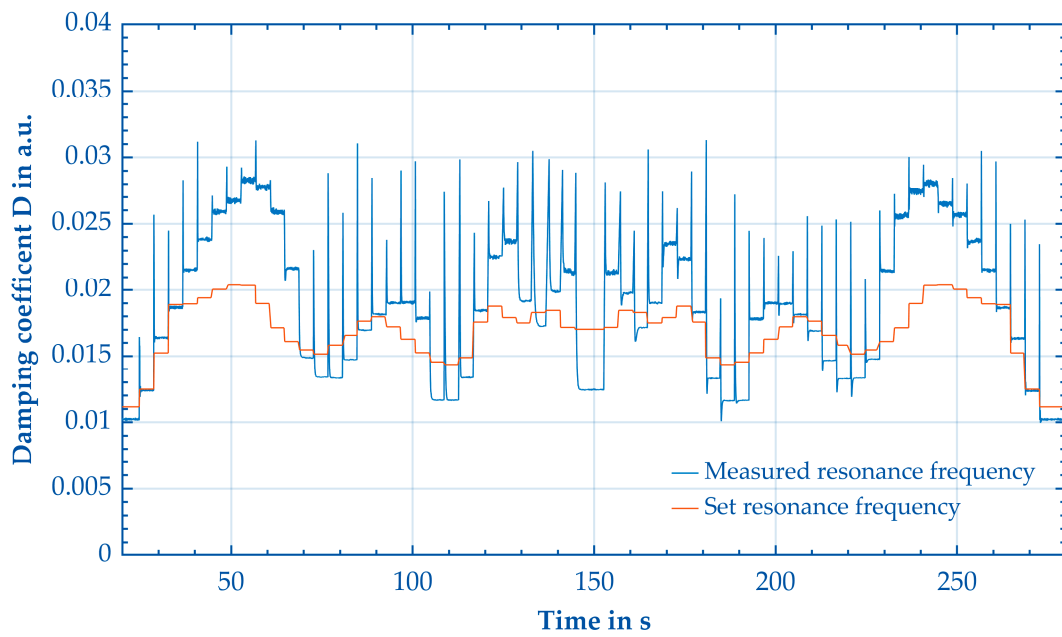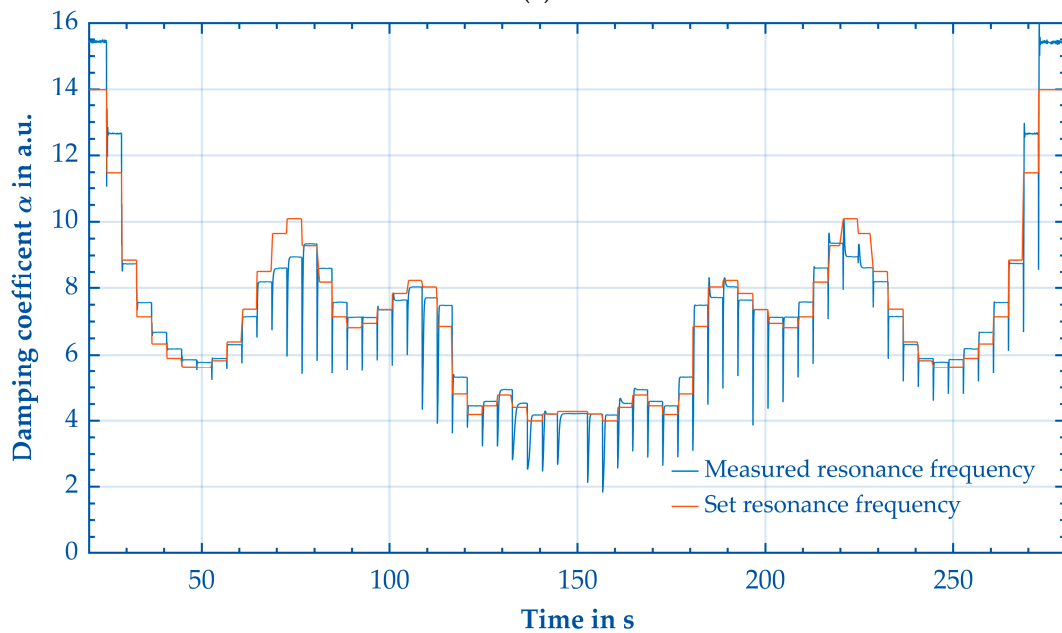
Figure 12. (**a**) Damping coefficient D derived from the measurements shown in Figure 11 compared to the true damping coefficient D; (**b**) damping coefficient α derived from the measurement shown in Figure 11 compared to the true damping coefficient α.

As can be seen, the parameters approach a constant value after each step, which corresponds to the qualitative progression of the expected values in some areas. However, high deviations for the damping coefficients D and α in the form of spikes during the adjustment process of the tracking electronics to the newly set resonance frequency of the adjustable resonator can be observed, presumably resulting from an incorrect assumption of the resonance frequency at these points in time due to the control's time constant in response to a resonance frequency step.

Furthermore, it becomes evident that especially the calculated damping factor D exhibits considerable discrepancies from the expected value. The propagation of errors

associated with the imprecise measurement of attenuation and the fitting process plays a pivotal role in this regard. The largest absolute deviations, occurring at approximately 50 s and 250 s, may be attributed to the fact that the amplitude response of the tracking electronics, as illustrated in Figure 9, exhibits the greatest deviations in the frequency range from 250 MHz to 300 MHz in comparison to the reference measurements conducted with the VNA. Thus, the reflection-induced errors cause, especially in these points, the fit of the attenuation parameter to deviate significantly from the expected value. If the reflection-induced errors in the measurement of the attenuations are minimized, the outcome of the fitting process and, consequently, the determined attenuation factors will also improve. This will be addressed next.

4. Conclusions

In this study, we introduce a new concept for the continuous tracking of the resonance frequency as well as attenuation at resonance and quality factor of an electrical resonator. The concept uses a radio frequency signal with a center frequency and two sidebands in the frequency range of the resonator, thereby enabling the individual demodulation of all signals. Due to the symmetry of the resonator, the sidebands have identical amplitudes, while the center frequency corresponds to the resonance frequency of the resonator. Consequently, any shift in the resonance frequency results in changes in the measured attenuation of the two sidebands, prompting the error signal for the controller to readjust all three signals to the new resonance frequency.

Moreover, the demodulated amplitudes of the sidebands and center frequency can be used to determine the quality factor and attenuation of the resonator under test. To show the feasibility of the concept, corresponding electronics were developed and tested with an adjustable resonator dummy. The experimental results demonstrate that the concept operates effectively, although with minor deviations in the measured resonance frequency and amplitude. These deviations primarily arise from the signal reflection present in the first setup of the tracking electronics. The measurement times could be reduced from several seconds up to minutes using a VNA (depending on the settings and analyzed frequency range) to 50 ms using the concept and electronics presented here.

While the current setup predominantly employs analog components for straightforward implementation, it holds the potential for digitization with the integration of sufficiently fast digital-to-analog converters and analog-to-digital converters. The analog electronics presented here allow the resonance frequency to be tracked in the range of 200 MHz to 1 GHz with an adjustable bandwidth of 8 MHz to 21.4 MHz. The maximum resolution of the measured resonance frequency is 1 kHz. The resolution of the resonance frequency is highly dependent on the noise of the two sidebands, as this noise directly leads to a control deviation, which then leads to the noise of the tracked resonance frequency. Furthermore, this noise of the tracked resonance frequency also affects the determination of the attenuation. For the electronics presented in this work, the standard deviation of the noise of the upper sideband is 0.04 dB, and it is 0.02 dB for the lower sideband. However, the presented method is limited to resonators with a certain quality factor, depending on the above-mentioned bandwidth range. Here, the adjustable bandwidth range of 8 MHz to 21.4 MHz is designed for resonators with a quality factor of 10 to 125. In addition, the presented method reaches its limits if the symmetry of the resonance curve of the measured resonator changes significantly over the frequency range considered or has multiple resonances in the same frequency range. However, given a suitable resonator, the specifications of the analog electronics presented in this work can be extended and the resonance frequency resolution can be further improved by further digitizing the concept, which will be part of future work.

Appendix A

Equation (1) can be derived from the transfer function A1 derived from the equivalent circuit of an SRR as shown in Figure 1b.

$$
\begin{aligned}
G(j\omega) = \frac{U_a}{U_e} &= \frac{\frac{1}{j\omega C_S} + R_{SRR} + j\omega L_{SRR}}{\frac{1}{j\omega C_S} + R_{SRR} + R_L + j\omega L_{SRR}} \\
&= \frac{j^2 \omega^2 L_{SRR} C_S + j\omega R_{SRR} C_s + 1}{j^2 \omega^2 L_{SRR} C_S + j\omega (R_{SRR} C_s + R_L C_s) + 1}
\end{aligned}
\tag{A1}
$$

The definition of the resonance frequency ω_0 and the damping coefficient D of a series resonant circuit, as shown in Equation (A2), leads to the transfer function presented in Equation (A3).

$$
\omega_0 = \frac{1}{\sqrt{L_{SSR} C_S}} \qquad D = \frac{R_{SRR}}{2} \cdot \sqrt{\frac{C_S}{L_{SRR}}}
\tag{A2}
$$

$$
G(j\omega) = \frac{j^2 \omega^2 \frac{1}{\omega_0^2} + j\omega \frac{2D}{\omega_0} + 1}{j^2 \omega^2 \frac{1}{\omega_0^2} + j\omega \left(1 + \frac{R_L}{R_{SRR}}\right) \frac{2D}{\omega_0} + 1} = \frac{1 - \omega^2 \frac{1}{\omega_0^2} + j\omega \frac{2D}{\omega_0}}{1 - \omega^2 \frac{1}{\omega_0^2} + j\omega \alpha \frac{2D}{\omega_0}}
\tag{A3}
$$

The amplitude response $|G(j\omega)|$ according to Equation (A4) can be obtained from Equation (A3). This finally leads to Equation (1).

$$
|G(j\omega)| = \frac{\sqrt{\omega^4 + (4D^2 - 2)\omega_0^2 \omega^2 + \omega_0^4}}{\sqrt{\omega^4 + (4\alpha^2 D^2 - 2)\omega_0^2 \omega^2 + \omega_0^4}} = \frac{\sqrt{\left(\omega_0^2 - \omega^2\right)^2 + (\omega \omega_0 2D)^2}}{\sqrt{\left(\omega_0^2 - \omega^2\right)^2 + (\alpha \omega \omega_0 2D)^2}}
\tag{A4}
$$

The photo in Figure A1 shows the assembled tracking electronics, including the test signal generation and the demodulation section for measuring the attenuation.
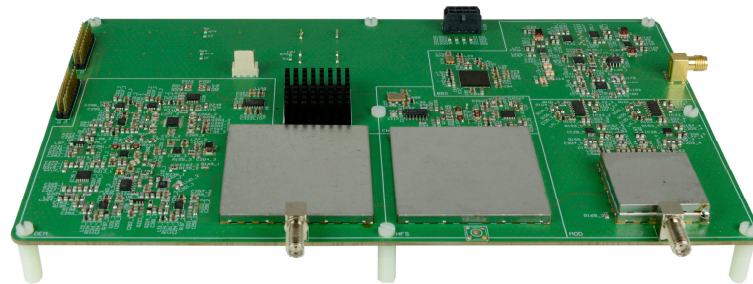
Figure A1. Picture of the tracking electronic.

The photo in Figure A2 shows the measurement setup containing the tracking electronics, the microcontroller evaluation board for data acquisition and resonance frequency control, and the resonator dummy.

The output power of the center frequency of the tracking electronics was measured over the frequency range from 200 MHz to 550 MHz with a Keysight Technologies N9030A PXA Signal Analyzer including the phase noise application Keysight Technologies N9068EMOD with software version A.24.57. Figure A3 shows that the amplitude of the output power decreases only slightly from −15.05 dBm at 200 MHz to −15.7 dBm at 550 MHz.
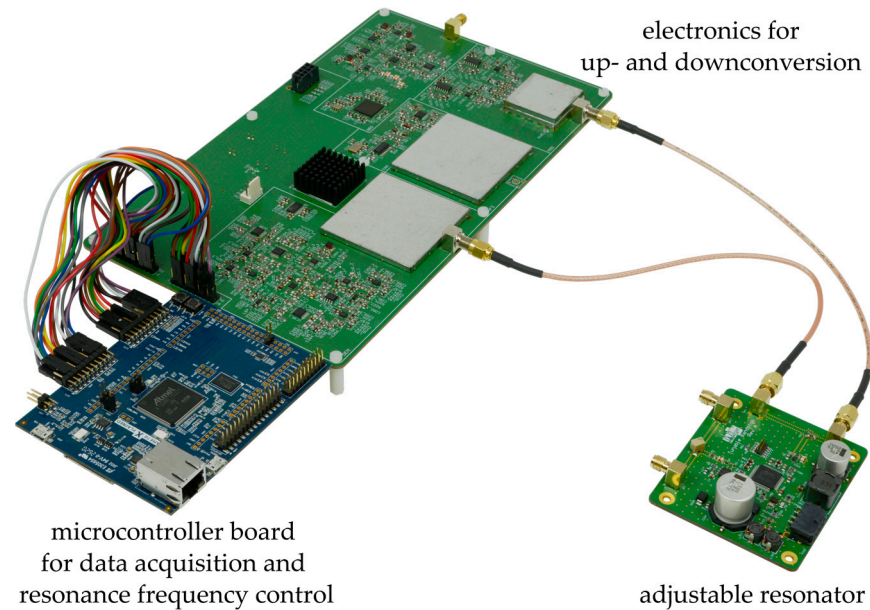
Figure A2. Picture of the developed measurement setup for investigating the resonance frequency and attenuation of a resonator dummy.
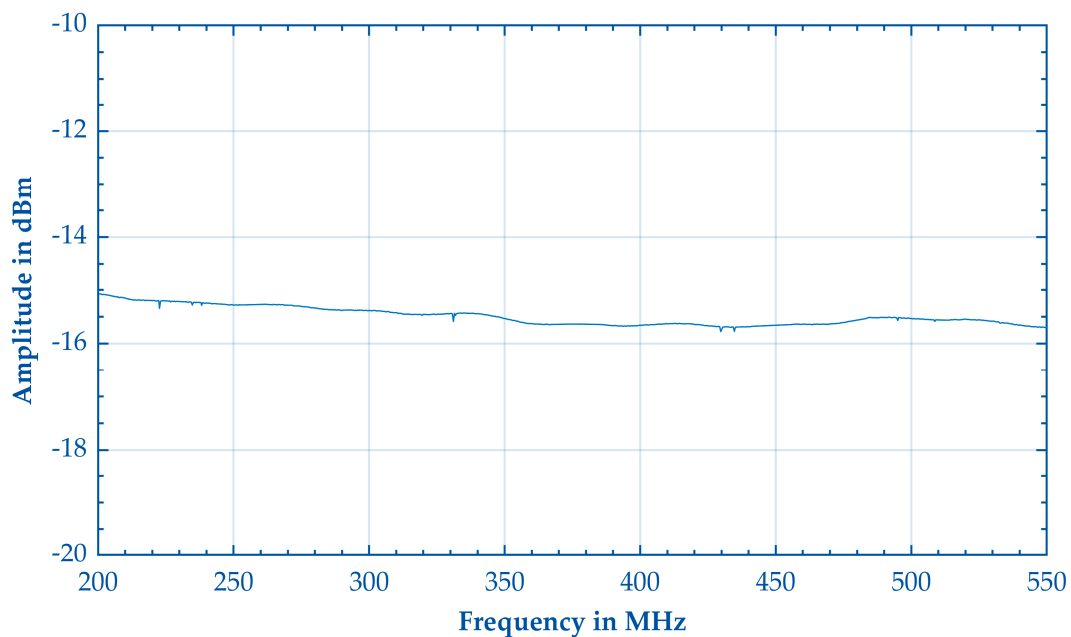
Figure A3. Output power of the center frequency of the tracking electronics.

Figure A4 shows the measurement result of a constant −15 dB damping element consisting of multiple damping elements from the Agilent Technology 11583C damping

set. The damping element was connected to the tracking electronics using two 25 cm SMA cables. The measured attenuation using the tracking electronics varies from -14 dB to -17 dB.
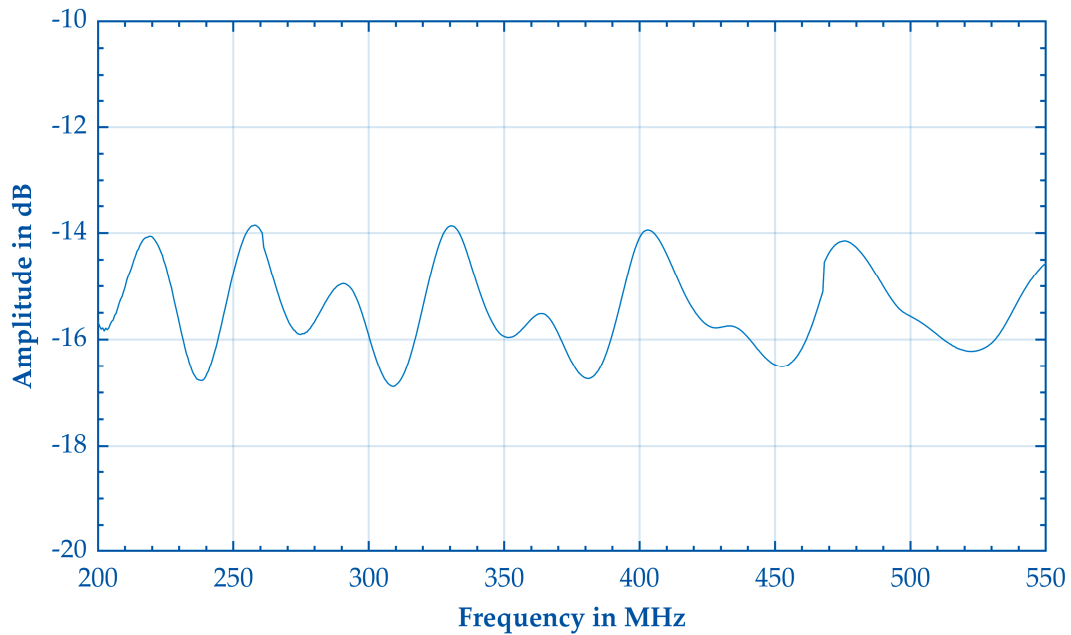
Figure A4. Measured attenuation of a constant -15 dB damping element.

Figure A5 shows the amplitude response of 16 of the 32 settings of the resonator dummy measured with the tracking electronics when connected via two 50 cm cables. Compared to the measurement in Figure 9, the maximum attenuation and also the shape of the amplitude responses change.
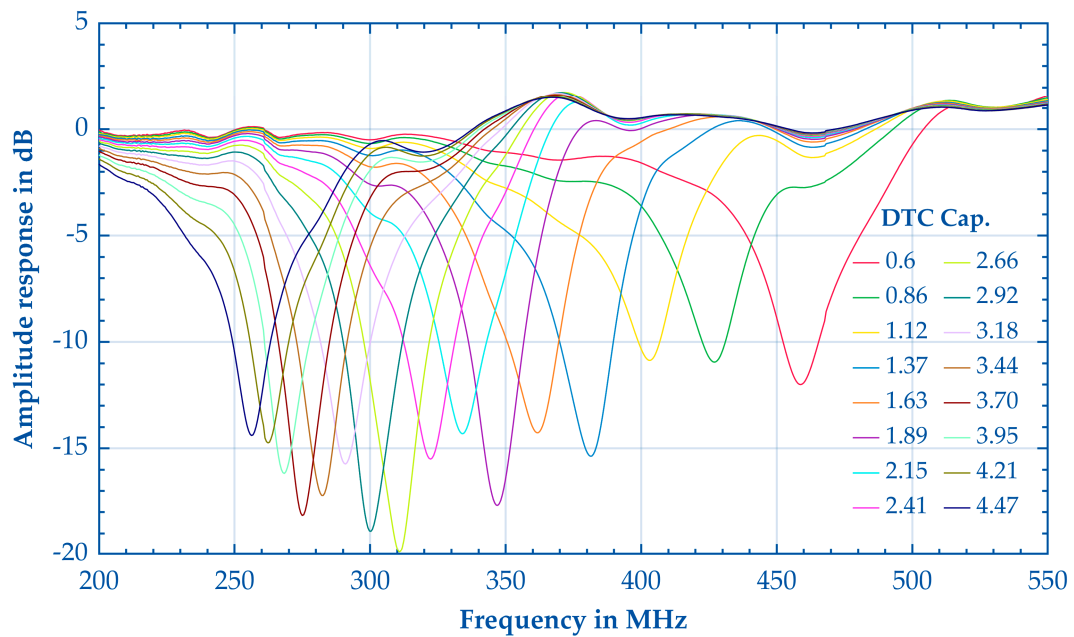
Figure A5. Amplitude responses of the resonator dummy at different DTC settings measured with the tracking electronics connected with two 50 cm SMA cables.

The measurements for the following two figures were conducted using the VNA ZNL6. Figure A6 shows the impedance parameter Z_{11} of the resonator dummy terminated with 50 ohm.
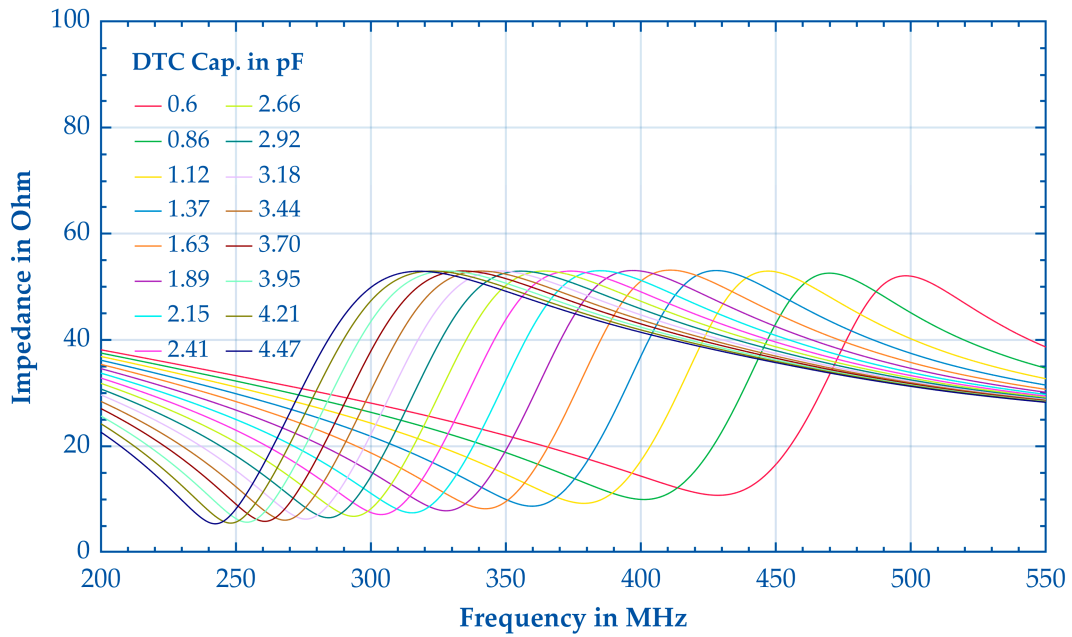
Figure A6. Impedance Z_{11} of the resonator dummy terminated with 50 ohms.

Figure A7 shows the results of measuring the impedance parameter Z_{11} of the resonator dummy terminated with the demodulation stage of the tracking electronics connected using a 25 cm SMA cable.
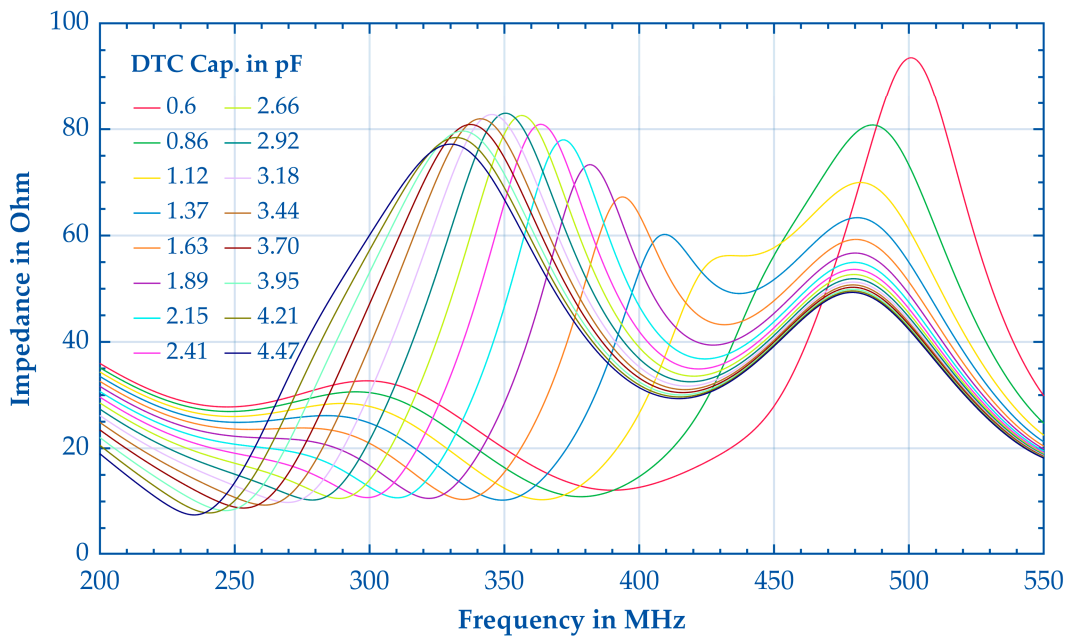
Figure A7. Impedance Z_{11} of the resonator dummy terminated with the demodulation stage of the tracking electronics.

Figure A8 shows the input impedance of the demodulation stage of the tracking electronics measured using the same VNA ZNL6.
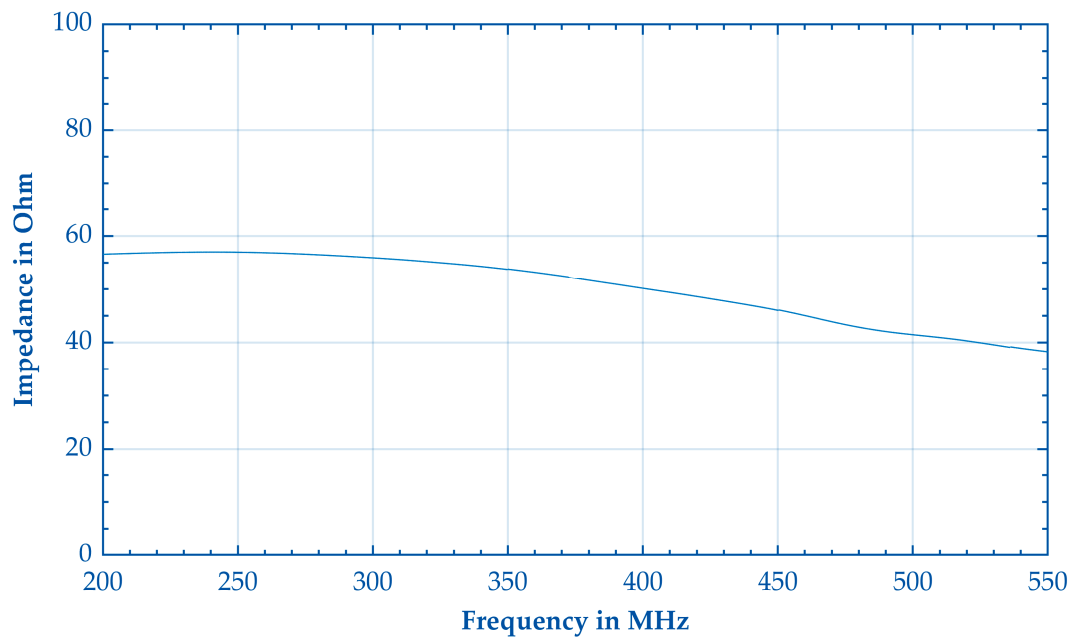
Figure A8. Input impedance of the demodulation stage of the tracking electronics.

Figure A9 shows the discrepancies between the expected resonance frequency and the resonance frequency determined by the tracking electronics in resonance frequency tracking mode derived from the measurement results shown in Figure 11.
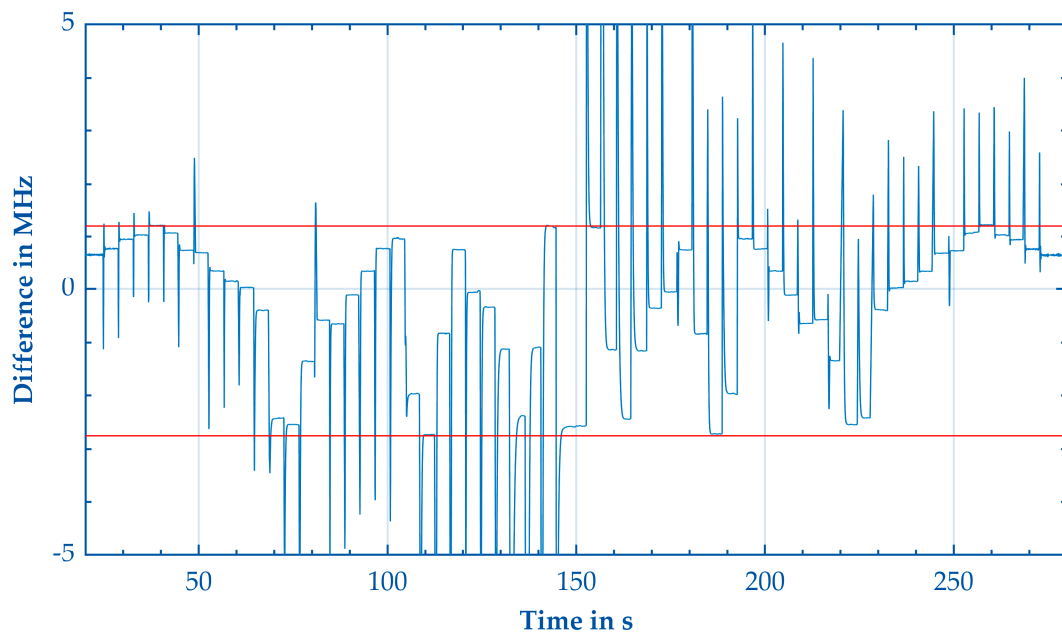
Figure A9. Difference between the expected resonance frequency and the resonance frequency determined by the tracking electronics in resonance frequency tracking mode. The red lines represent the maximum deviation of the resonance frequency from the expected resonance frequency with the frequency tracking settled.

References

1. Chuma, E.L.; Iano, Y.; Fontgalland, G.; Bravo Roger, L.L. Microwave Sensor for Liquid Dielectric Characterization Based on Metamaterial Complementary Split Ring Resonator. *IEEE Sens. J.* **2018**, *18*, 9978–9983. [CrossRef]
2. Viskadourakis, Z.; Fanourakis, G.; Tamiolakis, E.; Theodosi, A.; Katsara, K.; Vrithias, N.R.; Tsilipakos, O.; Kenanakis, G. Fabrication of mm-Scale Complementary Split Ring Resonators, for Potential Application as Water Pollution Sensors. *Materials* **2023**, *16*, 5290. [CrossRef]
3. Albishi, A.; Ramahi, O.M. Detection of surface and subsurface cracks in metallic and non-metallic materials using a complementary split-ring resonator. *Sensors* **2014**, *14*, 19354–19370. [CrossRef]
4. Verma, A.; Bhushan, S.; Tripathi, P.N.; Goswami, M.; Singh, B.R. A defected ground split ring resonator for an ultra-fast, selective sensing of glucose content in blood plasma. *J. Electromagn. Waves Appl.* **2017**, *31*, 1049–1061. [CrossRef]
5. Lee, H.-J.; Lee, H.-S.; Yoo, K.-H.; Yook, J.-G. DNA sensing using split-ring resonator alone at microwave regime. *J. Appl. Phys.* **2010**, *108*, 14908. [CrossRef]
6. Camli, B.; Kusakci, E.; Lafci, B.; Salman, S.; Torun, H.; Yalcinkaya, A. A Microwave Ring Resonator Based Glucose Sensor. *Procedia Eng.* **2016**, *168*, 465–468. [CrossRef]
7. Withayachumnankul, W.; Jaruwongrungsee, K.; Tuantranont, A.; Fumeaux, C.; Abbott, D. Metamaterial-based microfluidic sensor for dielectric characterization. *Sens. Actuators A Phys.* **2013**, *189*, 233–237. [CrossRef]
8. Dehning, K.J.; Hitzemann, M.; Gossmann, A.; Zimmermann, S. Split-Ring Resonator Based Sensor for the Detection of Amino Acids in Liquids. *Sensors* **2023**, *23*, 645. [CrossRef] [PubMed]
9. Dehning, K.J.; Hitzemann, M.; Zimmermann, S. Split-ring resonator with interdigital Split electrodes as detector for liquid and ion chromatography. *Sens. Bio-Sens. Res.* **2024**, *44*, 100645. [CrossRef]
10. Puentes, M.; Weiß, C.; Schüßler, M.; Jakoby, R. Sensor Array Based on Split Ring Resonators for Analysis of Organic Tissues. In Proceedings of the IEEE MTT-S International Microwave Symposium, Baltimore, MD, USA, 5–10 June 2011; pp. 1–4. [CrossRef]
11. Naqui, J.; Durán-Sindreu, M.; Martín, F. Alignment and Position Sensors Based on Split Ring Resonators. *Sensors* **2012**, *12*, 11790–11797. [CrossRef]
12. Ye, W.; Wang, D.-W.; Wang, J.; Wang, G.; Zhao, W.-S. An Improved Split-Ring Resonator-Based Sensor for Microfluidic Applications. *Sensors* **2022**, *22*, 8534. [CrossRef] [PubMed]
13. Sayed, M.; Ferrero, A.; Teppati, V. *Modern RF and Microwave Measurement Techniques*; Cambridge University Press: Cambridge, UK, 2013; ISBN 9781139567626.
14. Hitzemann, M.; Dehning, K.J.; Gehl, A.V.; Sterr, E.-F.; Zimmermann, S. Fast Readout of Split-Ring Resonators Made Simple and Low-Cost for Application in HPLC. *Electronics* **2022**, *11*, 1139. [CrossRef]
15. Tumurbaatar, B.; Kim, M.-J.; Park, C.-H.; Kim, C.S. A portable and computer-simulation analysis for the real-time measurement of the QCMD systems for the biomedical application. *Sens. Bio-Sens. Res.* **2018**, *21*, 75–81. [CrossRef]
16. Alassi, A.; Benammar, M.; Brett, D. Quartz Crystal Microbalance Electronic Interfacing Systems: A Review. *Sensors* **2017**, *17*, 2799. [CrossRef] [PubMed]
17. Wahab, M.F.; Dasgupta, P.K.; Kadjo, A.F.; Armstrong, D.W. Sampling frequency, response times and embedded signal filtration in fast, high efficiency liquid chromatography: A tutorial. *Anal. Chim. Acta* **2016**, *907*, 31–44. [CrossRef] [PubMed]
18. Kuzikov, S.; Avrakhov, P.; Jing, C.; Kostin, R.; Powers, T.; Rimmer, R.; Yakovlev, V.; Zhao, Y. (Eds.) A Method for In-Situ Q_0 Measurements of High-Quality SRF Resonators. In Proceedings of the 20th International Conference on RF Superconductivity, SRF2021, East Lansing, MI, USA, 28 June–2 July 2021; JACoW Publishing: Geneva, Switzerland, 2022.
19. Drever, R.W.P.; Hall, J.L.; Kowalski, F.V.; Hough, J.; Ford, G.M.; Munley, A.J.; Ward, H. Laser phase and frequency stabilization using an optical resonator. *Appl. Phys. B* **1983**, *31*, 97–105. [CrossRef]
20. Black, E.D. An introduction to Pound–Drever–Hall laser frequency stabilization. *Am. J. Phys.* **2001**, *69*, 79–87. [CrossRef]
21. Lippmann, M.; Hermeling, L.; Hitzemann, M.; Dehning, K.J.; Zimmermann, S. Electronics for Continuously Measuring the Resonance Frequency and Attenuation of a Split-Ring Resonator. In Proceedings of the 16 Dresdner Sensor-Symposium, Dresden, Germany, 5–7 December 2022; pp. 177–182.
22. Proksch, R. Multifrequency, repulsive-mode amplitude-modulated atomic force microscopy. *Appl. Phys. Lett.* **2006**, *89*, 113121-1–113121-3. [CrossRef]
23. Gannepalli, A.; Yablon, D.G.; Tsou, A.H.; Proksch, R. Mapping nanoscale elasticity and dissipation using dual frequency contact resonance AFM. *Nanotechnology* **2011**, *22*, 355705. [CrossRef]
24. Rodriguez, B.J.; Callahan, C.; Kalinin, S.V.; Proksch, R. Dual-frequency resonance-tracking atomic force microscopy. *Nanotechnology* **2007**, *18*, 475504. [CrossRef]
25. Weaver, D. A Third Method of Generation and Detection of Single-Sideband Signals. *Proc. IRE* **1956**, *44*, 1703–1705. [CrossRef]
26. Pratt, G.A.; Nguyen, J. Distributed synchronous clocking. *IEEE Trans. Parallel Distrib. Syst.* **1995**, *6*, 314–328. [CrossRef]
27. Park, S.; Park, C.S. High-Speed CMOS Frequency Dividers with Symmetric In-Phase and Quadrature Waveforms. *J. Circuits Syst. Comput.* **2016**, *25*, 1630006. [CrossRef]